mater.scichina.com link.springer.com

Published online 14 March 2023 | https://doi.org/10.1007/s40843-022-2381-6
Sci China Mater 2023, 66(6): 2308–2316

Surfactant-free synthesis of ordered 1D/2D NiZn-LDH heterostructure through oriented attachment for efficient photocatalytic CO_2 reduction with nearly 100% CO selectivity

Tingshi Zhang[1,2†], Xin Zhao[1,2†], Mingxiong Lin[1,2], Bixia Yang[1,2], Jiawei Yan[1,2], Zanyong Zhuang[1,2*] and Yan Yu[1,2*]

ABSTRACT **Ordered assembly of anisotropic one-dimensional (1D) and 2D nanomaterials is necessary for preparing delicate heterostructures with close contact to alleviate the energy and environmental crisis. Here, we exploited oriented attachment, a non-classical growth mechanism, as a tool for preparing ordered 1D/2D NiZn layered double hydroxide (NiZn LDH) heterostructures beyond the use of surfactants. Lattice matching between the (101) plane of 1D nanoneedles (NNs) and the (100) plane of 2D nanosheets (NSs) drives the spontaneous ordered assembly of 1D NiZn-LDH NNs on 2D NiZn-LDH NSs. Accordingly, the oxygen-deficient 1D NiZn-LDH capable of CO_2 adsorption is, therefore, well dispersed on the 2D platform. The oriented assembly generates strong and intimate interactions between the 1D and 2D units, enabling the efficient transfer of photogenerated electrons from 2D to 1D NiZn-LDH. The oriented 1D/2D NiZn-LDH heterostructure demonstrates superior CO_2 photoreduction performance under visible light irradiation, with a CO yield rate of 16,950 μmol g^{-1} h^{-1} and a 100% CO selectivity. The findings demonstrate that the growth of anisotropic nanomaterials can be tailored for advanced heterostructure design through oriented attachment alone.**

Keywords: ordered heterostructure, CO_2 photoreduction, oriented attachment, 1D/2D materials, lattice match

INTRODUCTION

Heterostructures composed of anisotropic nanomaterials constitute one of the most intriguing categories of catalysts in contemporary science and industry [1]. A growing number of studies have investigated the use of one-dimensional (1D)/2D materials as next-generation heterogeneous photocatalysts [2,3] for hydrogen production [4], water splitting [5], pollutant scavenging [6], and CO_2 reduction [7,8]. With these fascinating heterostructures, researchers seek to benefit from (1) the fast charge-carrier mobility along the 1D structure, (2) the confinement of electrons within the 2D structure, thereby suppressing charge recombination, and (3) the high surface-to-volume ratio of the 1D and 2D materials [9–13]. The catalytic activity of 1D/2D heterostructures is highly dependent on the close contact and strong interaction between mesoscale 1D and 2D building blocks [14–16]. The deposition of 1D materials on pre-synthesized 2D substrate by wet chemistry to create the 1D/2D hybrid typically has limited control over the 1D/2D assembly, and the 1D units are frequently irregularly arranged on the 2D substrates *via* weak interactions (e.g., electrostatic attraction) [9,17,18], as the morphologically anisotropic 1D and 2D nanomaterials have distinct growth environments and behaviors. Although some surfactants or polymers may be used to direct the assembly of 1D and 2D units [4,19–21], the organic additive frequently impairs the performance of the catalyst because it can poison the surface and create steric hindrances that are detrimental to charge transport and catalytic activity [8].

The fundamental difficulty in fabricating heterostructures is that the particle assembly of anisotropic building blocks to form an ordered structure must compete with the crystal growth of the same building blocks. For sufficiently small particles of several nanometers in size, the particle–particle attachment occurs due to the electrostatic (Coulombic) field surrounding the particles [22]. The calescence of particles into larger crystals, which is generally energetically advantageous, may follow the attachment and result in uniform crystal growth [23,24]. Nevertheless, during crystal growth, mesoscale repulsion can prevent large particles from coalescing and allow the assembly of anisotropic 1D or 2D units to produce heterostructures. The ordered assembly of large anisotropic particles is direction-dependent, and the alignment of mesoscale 1D and 2D nanomaterials requires their diffusion, rotation, and attachment, all of which are accompanied by substantial kinetic barriers. Consequently, the assembly of mesoscale particles relies heavily on the use of expensive, toxic surfactants (e.g., ethylenediaminetetraacetic acid [25], trimethylammonium bromide [26], sodium dodecylbenzene sulfonate [27], DNA [28,29]), as ligand–ligand attraction can provide the necessary driving force for directing the alignment of 1D and 2D units and thus the preferential adsorption on crystal surfaces [30].

Oriented attachment (OA), through which nanometer-scale

[1] College of Materials Science and Engineering, Fuzhou University, Fuzhou 350108, China
[2] Key Laboratory of Advanced Materials Technologies, Fuzhou University, Fuzhou 350108, China
[†] These authors contributed equally to this work.
[*] Corresponding authors (emails: zyzhuang@fzu.edu.cn (Zhuang Z); yuyan@fzu.edu.cn (Yu Y))

colloidal particles sharing the same crystallographic orientation can spontaneously form assembled architecture [31–35], is prevalent both in the formation of nature and in artificial nanosystems. Recently, we exploited the surfactant-free OA principle to assemble tiny 0D metal-organic frameworks (MOFs) with mesoscale 1D TiO_2 nanowires [36] and disperse tiny 0D CuO clusters on mesoscale 2D AlOOH nanosheets (NSs) [37], paving the way for further investigation of OA as a tool for complex material design. However, whether the OA principle can be applied to the ordered assembly of mesoscale 1D and 2D units to eliminate the need for surfactants remains unclear.

In this work, we disclosed a surfactant-free, spontaneous, and one-step strategy to fabricate an oriented 1D/2D heterostructure composed of anisotropic layered double hydroxides (LDHs) [38,39] of Ni and Zn, with sub-microscale 1D NiZn-LDH nanoneedles (NNs) arranged on 2D NiZn-LDH NSs in a defined orientation with intimate contact (Scheme 1). Due to their spontaneous lattice matching, the underlying mechanism was closely associated with the OA between the 1D NNs and the 2D NSs. Additionally, the developed system overcomes the known limitations of layered LDHs, that is, weak charge transfer ability and insufficient active edge sites [40–44]. The 1D/2D NiZn-LDH demonstrates excellent CO_2 photoreduction performance.

EXPERIMENTAL SECTION

Materials

Nickel(II) formate dihydrate was purchased from Aladdin Industrial Corporation. Meanwhile, nickel chloride hexahydrate ($NiCl_2{\cdot}6H_2O$), zinc chloride ($ZnCl_2$), and urea were purchased from Sinopharm Chemical Reagent Co., Ltd. All chemicals were of analytical grade and used as received without further purification. Deionized (DI) water with a resistivity of 18.2 MΩ cm was prepared using a Millipore Milli-Q purification system.

Synthesis of 2D NiZn-LDH and 1D/2D NiZn-LDH

Nickel chloride hexahydrate (5.94 g), zinc chloride (0.68 g) and urea (1.8 g) were dispersed ultrasonically in methanol (50 mL) for 30 min to give a suspension, which was then subjected to hydrothermal treatment at 120°C for 4 h. The precipitate was filtered, washed with DI water and ethanol, and then freeze-dried in vacuum for 12 h to give the 1D/2D NiZn-LDH. The 2D NiZn-LDH was produced by conducting the hydrothermal treatment at 120°C for 1 h using otherwise identical procedures.

Characterization

X-ray diffraction (XRD) patterns were obtained to analyze the crystal structures using a PANalytical X'pert MPD X-ray diffractometer (Panaco, Netherlands) with Cu Kα radiation (λ = 1.5406 Å) at 36 kV and 30 mA in a continuous scanning mode. The spectra were recorded at 5° min^{-1} with a step size of 0.01° over 2θ = 5°–65°. The morphology and size of the samples were examined using a Philips XL30 scanning electron microscope (SEM) and transmission electron microscope (TEM Titan G2 60-300, FEI, USA, with probe corrector). Elemental energy-dispersive spectroscopy (EDS) measurements were carried out using an FEI Tecnai F30 (USA) microscope at 300 kV. Meanwhile, a PHI 5000 Versa Probe spectrometer (Thermo Fisher Scientific, USA) was used to record the X-ray photoelectron spectrum (XPS). The Brunauer-Emmett-Teller (BET, ASAP 2460) method was used to calculate the specific surface area. The electron paramagnetic resonance (EPR) experiments for radical detection were carried out on a Bruker A300 spectrometer (Germany) with 5,5-dimethyl-1-pyrroline-*N*-oxide (DMPO) as the spin-trapping agent. The thermogravimetric and differential scanning calorimetry (TG-DSC) analyses were performed on a Setaram Setsys 16/18 thermo-analyzer with an air flow rate of 10 K min^{-1}. The photoluminescence (PL) spectroscopy was observed using a FluoroMax-4 (Tianmei, China). N_2 adsorption-desorption measurements were conducted on a Tristar II 3020. The surface structures and pore distributions of all obtained materials were obtained using a specific surface area and pore size analyzer at 77 K. Ultraviolet-visible (UV-vis) diffuse reflectance spectroscopy (DRS) (Varian Cary 500 UV-vis spectrophotometer, Varian, USA) tests were carried out with an integrating sphere attachment ranging from 200 to 800 nm and $BaSO_4$ (AR 99.99%, Aladdin Bio-Tech) as a reflectance standard. The transient photocurrent measurements were performed on an electrochemical workstation (CHI-660C, Chenhua, China) using aqueous Na_2SO_4 (1 mol L^{-1}) as the electrolyte solution. Photocurrent test (*I-t*) was conducted on the F-doped tin oxide (FTO) glass filled with 0.5 mL dimethyl formamide (DMF) solution. Moreover, ParSTAT MC electrochemical workstation was used to perform Mott-Schottky tests or electrochemical impedance spectra (EIS) in 0.2 mol L^{-1} Na_2SO_4 solution or a mixed resolution of 5 mmol L^{-1} $K_3[Fe(CN)_6]$/5 mmol L^{-1} $K_4[Fe(CN)_6]$/0.1 mol L^{-1} KCl (AR, Sinopharm Group). ^1H nuclear magnetic resonance (NMR) spectra were obtained using a Bruker AVANCE III NMR spectrometer at 400 MHz and tetramethyl silane (TMS) as an internal standard. Meanwhile, $^{13}CO_2$ isotopic labeling was confirmed using a gas chromatography-mass spectrometer (GC-MS, GC-7890B, Agilent).

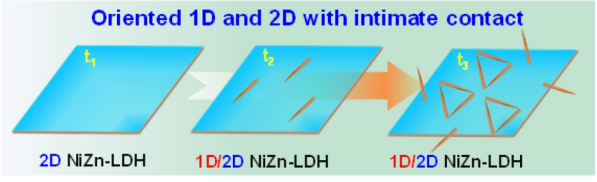

Scheme 1 Preparation of the 2D NiZn-LDH and the 1D/2D NiZn-LDH heterojunction.

Photocatalyzed CO_2 photoreduction reaction (CRR)

The photocatalytic CO_2 reduction was evaluated in a 25-mL quartz reactor (Zhengmao Glass Instrument Company, Fuzhou, China), where 1 mg catalyst and 8 mg $[Ru(bpy)_3]Cl_2{\cdot}6H_2O$ (abbreviated as **Ru**, bpy = 2,2′-bipyridine, Aladdin Biotech) were dispersed in a mixure of 2.0 mL water, 3.0 mL acetonitrile (MeCN) and 1.0 mL triethanolamine (TEOA). This system was thoroughly degassed and then backfilled with pure CO_2, repeated three times. Then the quartz reactor was put in the photocatalytic reaction system with a 300-W Xe lamp (>420 nm) at 25°C. After the reaction for a certain time, 0.5 mL product gases were analyzed by GC (GC-7890B, Agilent). $^{13}CO_2$ isotopic experiment was performed under the same conditions by replacing $^{12}CO_2$ gas with $^{13}CO_2$ and was measured by a GC-MS (Agilent 7890B and Agilent 5977B MSD). The cycle example was measured by adding fresh **Ru**.

The apparent quantum yield (AQY) was measured by using a 300-W Xe lamp with a wavelength of 450 nm. The number of incident photons was measured using a radiant power energy

meter (Ushio spectroradiometer, USR40). The AQY was calculated according to the following equation:

$$\mathrm{AQY(CO)} = \frac{2N(\mathrm{CO})}{\text{number of incident photons}} \times 100\% = \frac{2 \times M \times N_A \times \hbar \times c}{S \times P \times t \times \lambda} \times 100\%,$$

where M is the amount of CO molecules (mol), N_A is the Avogadro constant (6.022×10^{23} mol^{-1}), h is the Plank constant (6.626×10^{-34} J s), c is the speed of light (3×10^8 m s^{-1}), S is the irradiation area (cm^{-2}), P is the intensity of irradiation light (W cm^{-2}), t is the photoreaction time (s), and λ is the wavelength of the monochromatic light (m).

DFT calculation

All density functional theory (DFT) calculations were performed using the Vienna *ab initio* Simulation Package (VASP). The Perdew-Burke-Ernzerhof (PBE) functional within the generalized gradient approximation (GGA) method was used to describe the exchange-correlation effects. Meanwhile, the core-valence interactions were accounted for by the projected augmented wave (PAW) method. The energy cutoff for plane wave expansions was set to 450 eV, and the Brillouin zone integration was sampled using 2 × 2 × 1 Monkhorst-Pack grid *k*-points. The vacuum space was adopted 15 Å above the surfaces to avoid periodic interactions. The structural optimization was completed for energy and force convergence set at 1.0×10^{-4} eV and 0.02 eV Å^{-1}, respectively.

RESULTS AND DISCUSSION

Generation of the 1D/2D NiZn-LDH heterostructure

A one-pot surfactant-free synthesis at 120°C using $NiCl_2 \cdot 6H_2O$ (0.5 mol L^{-1}), $ZnCl_2$ (0.1 mol L^{-1}), and urea (0.6 mol L^{-1}) allows for the spontaneous formation of well-defined 1D/2D NiZn-LDH heterostructures *via* hydrothermal coprecipitation. The pure 2D NiZn-LDH (JCPDS No. 38-0715), which is composed of cross-linked thin 2D NSs weaved into ca. 16 μm microspheres (Fig. 1a), appears at about 1 h. In the SEM and TEM images (Fig. S1), the 2D NSs have a hexagonal hydrotalcite-like LDH phase that displays the (100) and (010) facets of NiZn-LDH, both with a *d*-spacing of 0.26 nm and an interfacial angle of 60°. The Ni, Zn, and O elements are distributed homogeneously in the NiZn-LDH NSs, as shown by the elemental mapping (Fig. S2).

The self-assembly of 1D NiZn-LDH NNs on 2D NiZn-LDH NSs begins around 2 h, and an increasing amount of 1D NNs become delicately decorated on the surfaces and edges of the pristine 2D NSs (Fig. 1b). The XRD analysis of a 1D/2D NiZn-LDH heterostructure shows no change in phase and still yields hexagonal NiZn-LDHs (Fig. 1d). Indeed, in the TG analysis (TGA), both 1D/2D NiZn-LDHs and the pristine 2D NiZn-LDHs have nearly the same weight loss (27–30 wt%) at 350°C (Fig. 1f), which is consistent with the TGA data of other NiZn-LDH structures reported in the literature [45,46].

Distinct orientations

The TEM images (Fig. 2a, b) show that the interplanar lattice spacing of the 2D NSs in the 1D/2D hybrid remains the same as in the pristine 2D NiZn-LDH. According to the fast Fourier transform (FFT) analysis of the TEM images, each individual NS is single crystalline (Fig. S1f). The selected area electron diffraction (SAED) results show that the {001} plane of the NS is exposed (Fig. S1c). The NiZn-LDH is also identified in the newly generated 1D NNs on 2D NSs. Elemental mapping (Fig. 1c) demonstrates that the elements of Ni, Zn, and O are distributed evenly throughout the entire 1D/2D microsphere as well as in domains with only 2D NSs. The *d*-spacings of the 1D NiZn-LDH NNs in the (006) and (101) planes are 0.39 and 0.26 nm, respectively (Fig. 2c, d), and the NNs grow along the <101> direction of the 1D NiZn-LDH. That is, the 1D and 2D NiZn-LDHs have different growth orientations in the 1D/2D heterostructure.

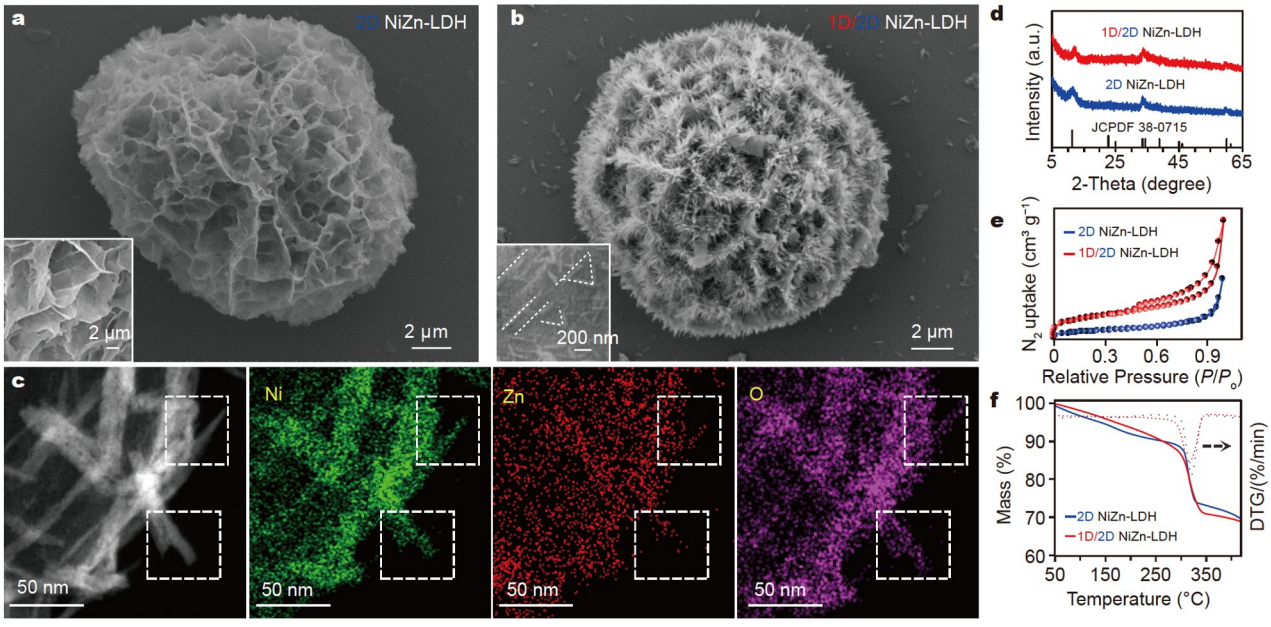

Figure 1 SEM images of (a) 2D NiZn-LDHs and (b) 1D/2D NiZn-LDHs. (c) EDX mapping of 1D/2D NiZn-LDHs. (d) XRD pattern, (e) BET, and (f) TG-differential thermal analysis (TG-DTA) spectra of 1D/2D NiZn-LDHs.

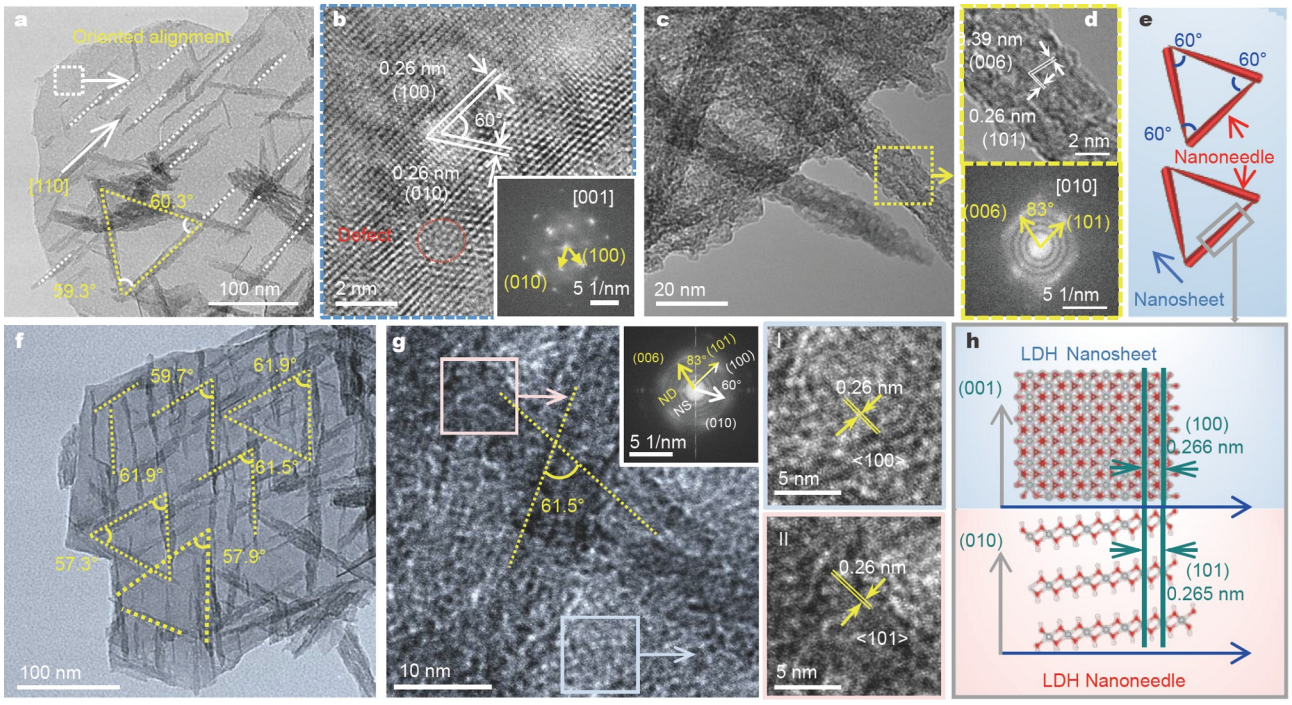

Figure 2 (a–d) TEM images of the 1D/2D NiZn-LDH. (e) Schematic illustration of the 1D/2D NiZn-LDH. (f, g) HRTEM images corresponding to the 1D NNs and 2D NSs, with the corresponding FFT in the inset. (h) Crystallographic parameters of the unit cells of the (001) and (010) planes of NiZn-LDHs.

Oriented growth of elongated 1D NNs on thin 2D NSs by lattice matching

The elongated 1D NiZn-LDH NNs, which are 75–260 nm in length and 6–24 nm in diameter (Fig. 2f), align themselves in a defined manner on the thin 2D NS surface. We discovered that when the reaction time is 2 h, only a small amount of the emerging 1D NNs are anchored on the surface of the pre-formed 2D NiZn-LDH. With the passage of time, the elongated NNs self-organize to form triangular architectures on the 2D NSs surface, intersecting at ca. 60° (Fig. 2e, f). The high-resolution TEM (HRTEM) image (Fig. 2g) shows that the <100> direction of the 2D NSs is parallel to the <101> direction of the 1D NNs, owing to the strong interfacial interaction between the highly crystalline NSs and NNs. The unit cell models (Fig. 2h) show that the (101) *d*-spacing of the 1D NNs (0.265 nm) is very close to the (100) *d*-spacing of the 2D NSs (0.266 nm). Furthermore, in the HRTEM image (Fig. S3), the {100} facets of the 2D NS are in parallel contact with the 101 facets of the 1D NN, forming a tightly-bonded interface. The attachment between 1D NNs and 2D NSs with a defined direction of the same *d*-spacing can be identified as an OA process. The OA growth mechanism can account for the assembly and good dispersion of sub-microscale 1D NNs on the 2D NSs with a defined orientation. According to the HRTEM images, the exposed surfaces of the 1D NNs and the 2D NSs of the NiZn-LDH are the (010) plane and the (001) plane, respectively.

The 1D/2D NiZn-LDH hybrid has a significantly larger surface area (115 $m^2 g^{-1}$) than the pristine 2D NiZn-LDH (46 $m^2 g^{-1}$) according to the N_2 adsorption-desorption isotherm (Fig. 1e), which can be attributed to the good dispersion and oriented assembly of the 1D NNs on the 2D NSs. Furthermore, we used XPS to examine the oxidation states of the elements in the 1D/2D hybrid, as the OA mechanism is known to cause defects due to imperfect particle alignment at the interface [37,47,48]. Ni exists mostly as Ni^{2+} (856.03 eV) in both the pristine 2D NiZn-LDH and the 1D/2D NiZn-LDH, with a trace amount of Ni^{3+} (857.69 eV) (Fig. 3a) [49], and Zn exists only as Zn^{2+} (Fig. 3b) [50,51]. The hydroxyl groups are responsible for the XPS signal of O 1s (Fig. S4) at 531.8 eV. The EPR of NiZn-LDHs was also measured to determine the presence of oxygen vacancies (OVs) in the LDHs. The EPR signal at $g = 2.004$, which is caused by electrons trapped in the OVs of the catalyst [52], is much stronger for the 1D/2D NiZn-LDH than for the 2D NiZn-LDH, indicating that the former has more OVs than the latter (Fig. 3c).

Strong CO_2 adsorption capacity

Fig. 4a shows that the CO_2 adsorption capacity of the 1D/2D hybrid (12.85 $cm^3 g^{-1}$) is twice that of the 2D NSs (6.97 $cm^3 g^{-1}$). We additionally ran theoretical calculations to examine the adsorption behavior of CO_2 on the exposed surface of the 1D NNs and the 2D NSs. Fig. 4e, f show that the adsorption energy of CO_2 on the NiZn-LDH is lower on the (010) plane (E_{ad} = −0.84 eV) than on the (001) plane (E_{ad} = −0.75 eV). That is, with its (010) plane exposed, the 1D NNs can provide more active sites for CO_2 capture.

Oriented electron injection from 2D to 1D NiZn-LDH

Using the 2D NSs as a reference, we then investigated the light-harvesting behavior and band structure of the 1D/2D hybrid. While both the 2D NSs and the 1D/2D hybrid respond to visible light (Fig. S5), the intensity of light adsorption is stronger for the 1D/2D hybrid because the presence of 1D NNs increases the amount of OVs [53]. Theoretical derivations from the Kubelka-Munk function and the Mott-Schottky plots (Fig. S6) show that the conduction bands of both the 2D NSs and the 1D/2D hybrid

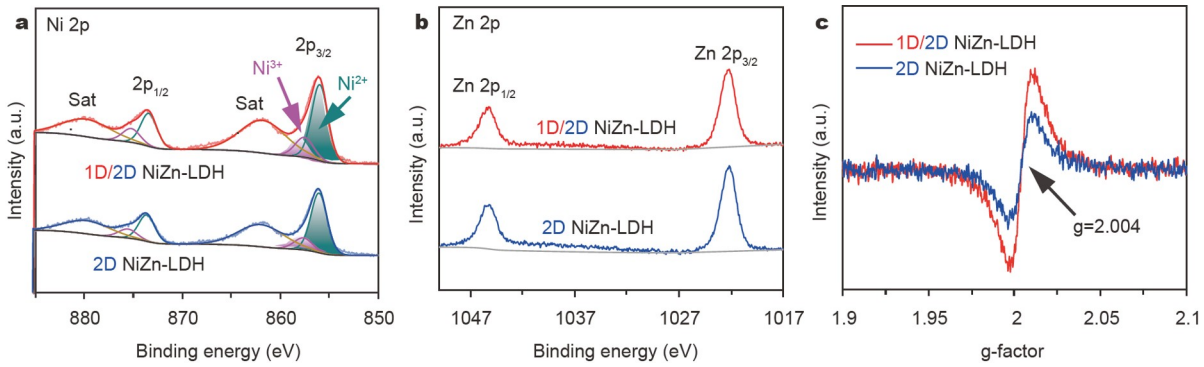

Figure 3 (a) Ni 2p XPS, (b) Zn 2p XPS, and (c) EPR spectra of 2D NiZn-LDHs and 1D/2D NiZn-LDHs.

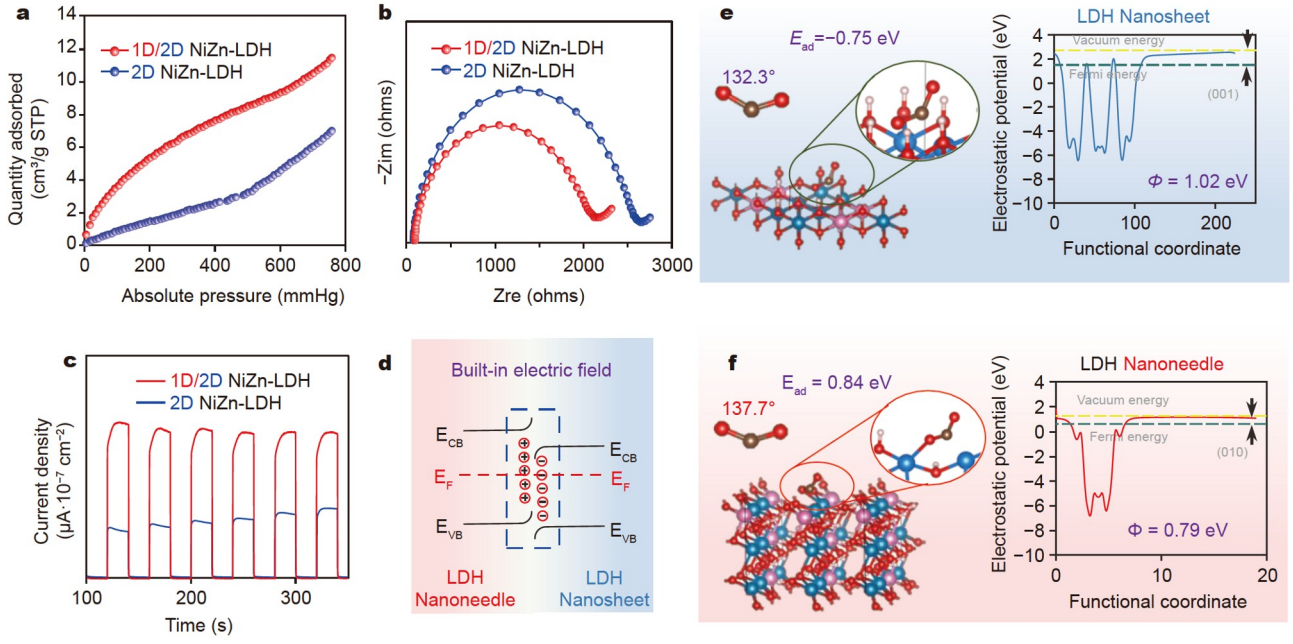

Figure 4 (a) CO_2 adsorption capabilities, (b) EIS Nyquist plots, and (c) photocurrents of 2D NiZn-LDHs and 1D/2D NiZn-LDHs. (d) Built-in electric fields of 2D NiZn-LDHs and 1D/2D NiZn-LDHs. (e, f) CO_2 adsorption energies and the electrostatic potentials of the (001) and (010) planes of NiZn-LDHs.

are suitable for the conversion of CO_2 to CO (−0.51 eV) and H_2O to H_2 (−0.41 eV). Based on the EIS, *I-t* data, and PL spectra, the charge transfer capability of the catalysts was then compared (Fig. 4b–d and Fig. S7). The 1D/2D hybrid has a much lower charge transfer resistance and a stronger photocurrent response than pure 2D NSs, allowing for superior carrier migration capability [54]. The lattice matching-driven ordered assembly of 1D NNs on 2D NSs can facilitate the transport of electrons from 2D NSs to the 1D NNs [55].

In theory, 1D nanostructures allow for rapid charge transfer along their axes, while 2D nanostructures can confine electrons in their unique atomic layers, both of which can promote charge transfer in the resulting 1D/2D heterostructure [56,57]. As the previous experiments demonstrated that CO_2 preferentially accumulates on the surface of the 1D NNs, it is critical to determine whether electrons can accumulate in the hybrid 1D NNs, as the direction of electron movement can vary in the heterostructure. In the Bi_2O_3/Bi_2WO_6 heterostructure, for example, electrons transfer from the 2D Bi_2O_3 NSs to the 1D Bi_2WO_6 nanowires [56], whereas in the graphene/CNs heterojunction, electrons transfer from the 1D carbon nitride (CN) nanorods to the 2D graphene [8]. Fermi energy can be used to calculate the charge transfer between two semiconductors. Fig. 4e, f show that work functions of the (001) and (010) planes of NiZn-LDHs are 1.02 and 0.79 eV, respectively, from which the Fermi energy can be calculated as follows:

$$\Phi = E_{vac} - E_F, \quad (1)$$

where Φ is the work function, E_{vac} and E_F are the electrostatic potential of vacuum energy and Fermi energy, respectively. Hence, the (010) plane of the NiZn-LDH has a higher Fermi energy than the (001) plane of the NiZn-LDH. Upon the formation of the heterostructure by attachment, the hybridization of the (001) and (010) planes of the NiZn-LDH will cause electron redistribution until their Fermi energies reach equilibrium. Consequently, the electron density decreases in the (010) plane and increases in the (001) plane, which generates a built-in electric field at the interface that can render the directed charge transfer from the (001) to (010) plane in the NiZn-LDH (Fig. 4d). The results of the selective Pt photo-deposition

experiment (Fig. S8) also confirm that electrons prefer to accumulate on the 1D NNs rather than the 2D NSs [37]. In the well-defined 1D/2D NiZn-LDH assembled architecture, electrons can therefore transfer from the 2D NSs to the 1D NNs, thereby creating a potential platform for CO_2 reduction.

Superior efficiency and selectivity in CO_2 reduction

CRR was carried out in CH_3CN/H_2O with the 1D/2D hybrid and 2D NSs as the catalysts, TEOA as an electron donor, and **Ru** as the visible-light photosensitizer. Fig. 5a, b show that the 1D/2D hybrid has nearly twice the CO yield (16,950 μmol h^{-1} g^{-1}) compared with the 2D NSs (9740 μmol h^{-1} g^{-1}) and outperforms many other CO_2 conversion systems with its superior CO yield (e.g., Ni-TpBpy, 811 μmol h^{-1} g^{-1}; Ni-covalent-organic frameworks (COFs), 5310 μmol h^{-1} g^{-1}; $NiCo_2O_4$ hollow nanocages (HCs), 10,500 μmol h^{-1} g^{-1}, Fig. S9, see detail in Table S1 [58–68]). The gas production and selectivity of 1D/2D NiZn-LDHs in CRR with different masses were investigated as a function of the number of catalytic sites participating in the catalytic reaction and the ability to accept excitation light and electrons [64] (Fig. S10). The highest CRR efficiency (V_{CO} = 16.95 μmol h^{-1}) is achieved with 1 mg of 1D/2D NiZn-LDHs while maintaining 100% CO selectivity.

The wavelength-dependent gas yield in accordance with the light absorption spectrum of **Ru** photosensitizer (Fig. S11) indicates that the CO_2 photoreduction starts from the light absorption of **Ru** [64,67]. Of note, 1D/2D NiZn-LDHs display a superior AQY of approximately 2.41% at 450 nm, better than many other reported photocatalytic systems under comparable conditions (Table S2). In addition, both the 2D NSs and the 1D/2D hybrid attain 100% CO selectivity, giving CO as the sole reaction product.

To identify the key factors in the CRR, we performed a series of control experiments (Fig. 5d). Currently, photoreduction systems rely primarily on the use of photosensitizers to generate enough photogenerated electrons for CO_2 photoreduction. When CRR was performed without **Ru** or TEOA, in the dark, or in N_2, negligible CO and H_2 were detected. As a result, the first step in developing CRR is to excite the photosensitizer. The catalytic redox reaction will occur on the catalyst due to the injection of electrons from the photosensitizer. To achieve peak performance, not only must CO_2 be adopted and activated on the catalyst, but also an efficient electron transfer to the catalytically active site should be present (Fig. 5d). As shown in Fig. S12, no liquid byproduct (e.g., CH_3OH and HCOOH) is formed as measured by ^1H NMR in the following redox reaction. The generated CO product must have originated from the CO_2 reactant, because when pure $^{13}CO_2$ is used as the carbon source, the product is ^{13}CO of m/z = 29 peak in the mass spectroscopy (Fig. 5c). Notice that the 1D/2D hybrid is also stable, giving minimal change in CO yield and nearly 100% CO selectivity after four catalytic cycles (Fig. S13), and the retrieved 1D/2D hybrid shows no phase or structural change in XRD and SEM (Fig. S14).

Impact on the rational design of delicate heterostructures

In materials science, manipulating the growth of fine particles for advanced catalyst design is rudimentary [69]. OA produces anisotropy in particle growth, whereas classical Ostwald ripening (OR) produces isotropy. Reported initially in 1998 [70], the OA mechanism has been demonstrated as a key driving force as well as a facile tool in the fabrication of delicate oxides (TiO_2 [71], SnO_2 [23], and ZnO [72]), hydroxides ($Cu(OH)_2$ [73]), carbonates ($NaY(CO_3)_2{\cdot}6H_2O$ and $(NH_4)Y(CO_3)_2{\cdot}H_2O$ [74]), sulfides (PbS [75] and $Cu_{1.94}S$ [76]), and various other compounds (e.g., $CsPbBr_3$ [77], PbSe [78], and Au [79]) catalysts. In principle, the OA mechanism can allow primary particles to self-organize into complex hierarchical architecture [70,72]. Extending the OA principle to engineer the spontaneous assembly of anisotropic 1D and 2D materials has the potential to significantly expand the

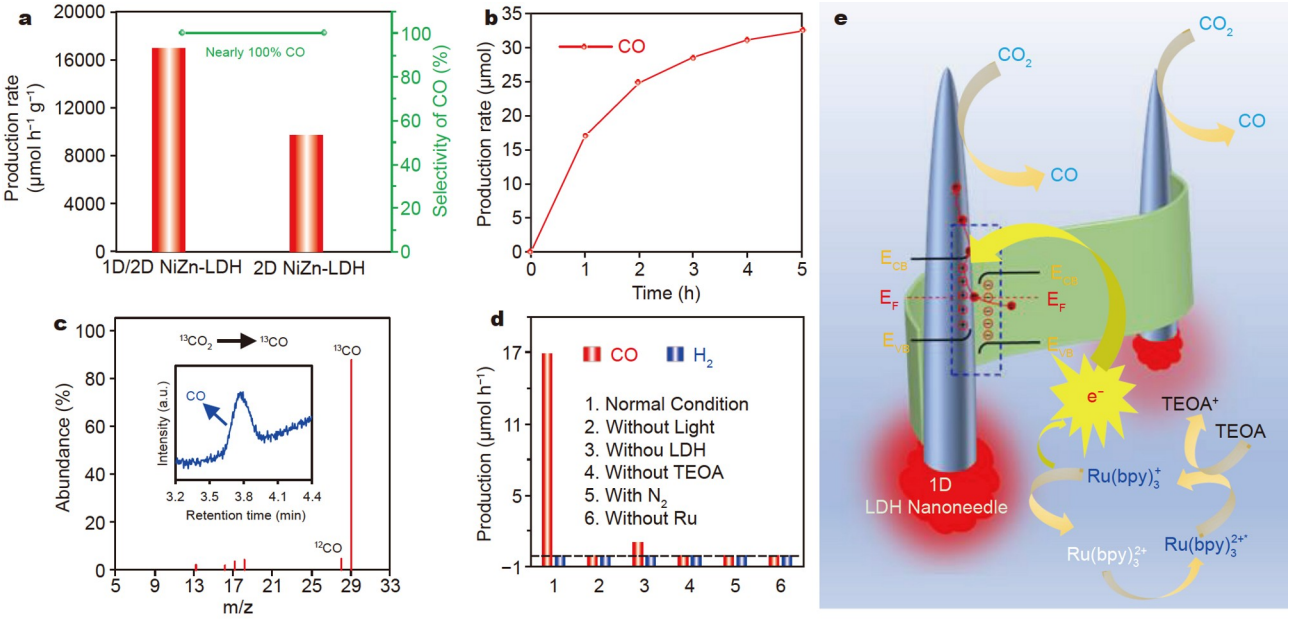

Figure 5 (a) CO_2 photoreduction performances over 2D and 1D/2D NiZn-LDHs. (b) Time-dependent CO evolution over 1D/2D NiZn-LDHs. (c) Mass spectrum of ^{13}CO (m/z = 29) produced over 1D/2D NiZn-LDHs in the photocatalytic reduction of pure $^{13}CO_2$. (d) Gas generation rates of the control experiments. (e) Proposed mechanism for the visible-light-driven CO_2 photoreduction catalyzed by 1D/2D NiZn-LDHs.

family of functional materials while avoiding the surface passivation caused by surfactants in conventional synthesis [69]. In this study, we discovered that in the absence of surfactant, the 1D NiZn-LDH that emerges on the 2D NiZn-LDH platform can self-organize in a defined and moderate manner thanks to OA. The (101) direction of the ordered 1D/2D LDH assembly can be parallel to the (100) direction of the pre-formed 2D LDH. The findings show that even when no surfactant or artificial control is used, inorganic nanomaterials can adjust their growth and assembly behavior to provide a delicate, sterically stable assembled architecture. Through the surfactant-free OA principle, the intimate attachment and strong interaction of mesoscale units allow access to complex catalysts with optimal physicochemical properties, chemical performance, and structural stability [69].

CONCLUSIONS

We demonstrated the oriented assembly of 1D and 2D NiZn-LDHs of morphologically anisotropic particles that can spontaneously regulate their growth directions in this work. Based on lattice matching, a large-scale, well-defined, ordered 1D/2D NiZn-LDH assembly composed of 1D NNs and 2D NSs was created, which has superior photocatalytic performance in the CRR (16,950 μmol g^{-1} h^{-1} CO yield and 100% CO selectivity). As shown in Fig. 5e, the presence of oxygen-deficient and orderly arranged 1D NNs can significantly improve CO_2 adsorption, while the built-in electric field at the 1D/2D interface can direct electron transfer from the 2D NSs to the 1D NNs. The findings may contribute to our understanding of OA as an appealing tool for advancing efficient catalyst design with different low-dimensional materials as building blocks.

Received 6 November 2022; accepted 27 December 2022; published online 14 March 2023

1 Chen PC, Liu M, Du JS, *et al.* Interface and heterostructure design in polyelemental nanoparticles. Science, 2019, 363: 959–964
2 Dang ZM, Zheng MS, Zha JW. 1D/2D carbon nanomaterial-polymer dielectric composites with high permittivity for power energy storage applications. Small, 2016, 12: 1688–1701
3 Bera A, Lin W, Yao Y, *et al.* ZnO nanorods on a $LaAlO_3$-$SrTiO_3$ interface: Hybrid 1D-2D diodes with engineered electronic properties. Small, 2016, 12: 802–809
4 Chen J, Wu XJ, Gong Y, *et al.* Edge epitaxy of two-dimensional $MoSe_2$ and MoS_2 nanosheets on one-dimensional nanowires. J Am Chem Soc, 2017, 139: 8653–8660
5 Xu B, He P, Liu H, *et al.* A 1D/2D helical CdS/$ZnIn_2S_4$ nano-heterostructure. Angew Chem Int Ed, 2014, 53: 2339–2343
6 Liu X, Wu L, Liu T, *et al. In situ* confine of Co_3ZnC/Co in N-doped carbon nanotube-grafted graphitic carbon nanoflakes as 1D-2D hierarchical catalysts toward superior redox activity. Appl Catal B-Environ, 2021, 281: 119513
7 Shi H, Chen G, Zhang C, *et al.* Polymeric g-C_3N_4 coupled with $NaNbO_3$ nanowires toward enhanced photocatalytic reduction of CO_2 into renewable fuel. ACS Catal, 2014, 4: 3637–3643
8 Xia Y, Tian Z, Heil T, *et al.* Highly selective CO_2 capture and its direct photochemical conversion on ordered 2D/1D heterojunctions. Joule, 2019, 3: 2792–2805
9 Adekoya D, Zhang S, Hankel M. 1D/2D C_3N_4/graphene composite as a preferred anode material for lithium ion batteries: Importance of heterostructure design *via* DFT computation. ACS Appl Mater Interfaces, 2020, 12: 25875–25883
10 Xiong P, Zhang X, Wan H, *et al.* Interface modulation of two-dimensional superlattices for efficient overall water splitting. Nano Lett, 2019, 19: 4518–4526
11 Jang SW, Dutta S, Kumar A, *et al.* Holey Pt nanosheets on NiFe-hydroxide laminates: Synergistically enhanced electrocatalytic 2D interface toward hydrogen evolution reaction. ACS Nano, 2020, 14: 10578–10588
12 Zhao X, Li Q, Xu L, *et al.* Interface engineering in 1D ZnO-based heterostructures for photoelectrical devices. Adv Funct Mater, 2021, 32: 2106887
13 Yang B, Zheng Y, Wen Y, *et al.* Sponge-like nickel carbonate of high porosity and carbonate vacancy for high-performance CO_2 photoreduction. Adv Sustain Syst, 2022, 6: 2100494
14 He Y, Jia L, Lu X, *et al.* Molecular-scale manipulation of layer sequence in heteroassembled nanosheet films toward oxygen evolution electrocatalysts. ACS Nano, 2022, 16: 4028–4040
15 Hu X, Zhang S, Sun J, *et al.* 2D Fe-containing cobalt phosphide/cobalt oxide lateral heterostructure with enhanced activity for oxygen evolution reaction. Nano Energy, 2019, 56: 109–117
16 Han X, Niu Y, Yu C, *et al.* Ultrafast construction of interfacial sites by wet chemical etching to enhance electrocatalytic oxygen evolution. Nano Energy, 2020, 69: 104367
17 Navarro-Pardo F, Liu J, Abdelkarim O, *et al.* 1D/2D cobalt-based nanohybrids as electrocatalysts for hydrogen generation. Adv Funct Mater, 2020, 30: 1908467
18 Nawaz A, Goudarzi S, Asghari MA, *et al.* Review of hybrid 1D/2D photocatalysts for light-harvesting applications. ACS Appl Nano Mater, 2021, 4: 11323–11352
19 Sun G, Li B, Li J, *et al.* Direct van der Waals epitaxial growth of 1D/2D Sb_2Se_3/WS_2 mixed-dimensional p-n heterojunctions. Nano Res, 2019, 12: 1139–1145
20 Wang Y, Yan L, Dastafkan K, *et al.* Lattice matching growth of conductive hierarchical porous MOF/LDH heteronanotube arrays for highly efficient water oxidation. Adv Mater, 2021, 33: 2006351
21 Wang W, Dong J, Ye X, *et al.* Heterostructured TiO_2 nanorod@nanobowl arrays for efficient photoelectrochemical water splitting. Small, 2016, 12: 1469–1478
22 Petek H. Single-molecule femtochemistry: Molecular imaging at the space-time limit. ACS Nano, 2014, 8: 5–13
23 Zhuang Z, Huang F, Lin Z, *et al.* Aggregation-induced fast crystal growth of SnO_2 nanocrystals. J Am Chem Soc, 2012, 134: 16228–16234
24 De Yoreo JJ, Gilbert PUPA, Sommerdijk NAJM, *et al.* Crystallization by particle attachment in synthetic, biogenic, and geologic environments. Science, 2015, 349: 6760
25 Akshay VR, Arun B, Suneesh MV, *et al.* Surfactant-induced structural phase transitions and enhanced room temperature thermoelectric performance in n-type Bi_2Te_3 nanostructures synthesized *via* chemical route. ACS Appl Nano Mater, 2018, 1: 3236–3250
26 Yin K, Chao Y, Lv F, *et al.* One nanometer PtIr nanowires as high-efficiency bifunctional catalysts for electrosynthesis of ethanol into high value-added multicarbon compound coupled with hydrogen production. J Am Chem Soc, 2021, 143: 10822–10827
27 Xia R, Chen S, Jiang S, *et al.* Monolayer amorphous carbon-bridged nanosheet mesocrystal: Facile preparation, morphosynthetic transformation, and energy storage applications. ACS Appl Mater Interfaces, 2021, 13: 1114–1126
28 Arasu V, Hwang S, Zhang B, *et al.* 1D fibers and 2D patterns made of quantum dot-embedded DNA *via* electrospinning and electrohydrodynamic jet printing. Adv Mater Technol, 2019, 4: 1800280
29 Kahn JS, Gang O. Designer nanomaterials through programmable assembly. Angew Chem Intl Edit, 2022, 61: e202105678
30 Zhang X, Shen Z, Liu J, *et al.* Direction-specific interaction forces underlying zinc oxide crystal growth by oriented attachment. Nat Commun, 2017, 8: 835
31 Lange AP, Samanta A, Olson TY, *et al.* Quantized grain boundary states promote nanoparticle alignment during imperfect oriented attachment. Small, 2020, 16: 2001423
32 Ding K, Gulec A, Johnson AM, *et al.* Identification of active sites in CO oxidation and water-gas shift over supported Pt catalysts. Science, 2015, 350: 189–192
33 Schliehe C, Juarez BH, Pelletier M, *et al.* Ultrathin PbS sheets by two-dimensional oriented attachment. Science, 2010, 329: 550–553
34 Zhang Y, Chen B, Guan D, *et al.* Thermal-expansion offset for high-

performance fuel cell cathodes. Nature, 2021, 591: 246–251
35 Coropceanu I, Janke EM, Portner J, *et al.* Self-assembly of nanocrystals into strongly electronically coupled all-inorganic supercrystals. Science, 2022, 375: 1422–1426
36 Lin M, Jiang W, Yang C, *et al.* Oriented assembly of metal-organic frameworks and deficient TiO_2 nanowires directed by lattice matching for efficient photoreversible color switching. Sci China Mater, 2021, 65: 992–999
37 Zhang T, Yang C, Li B, *et al.* Atomically dispersed and oxygen deficient CuO clusters as an extremely efficient heterogeneous catalyst. Nanoscale, 2022, 14: 4957–4964
38 Zhou D, Cai Z, Lei X, *et al.* NiCoFe-layered double hydroxides/N-doped graphene oxide array colloid composite as an efficient bifunctional catalyst for oxygen electrocatalytic reactions. Adv Energy Mater, 2018, 8: 1701905
39 Zhou D, Xiong X, Cai Z, *et al.* Flame-engraved nickel-iron layered double hydroxide nanosheets for boosting oxygen evolution reactivity. Small Methods, 2018, 2: 1800083
40 Lv J, Wang L, Li R, *et al.* Constructing a hetero-interface composed of oxygen vacancy-enriched Co_3O_4 and crystalline-amorphous NiFe-LDH for oxygen evolution reaction. ACS Catal, 2021, 11: 14338–14351
41 Zheng F, Zhang W, Zhang X, *et al.* Sub-2 nm ultrathin and robust 2D FeNi layered double hydroxide nanosheets packed with 1D FeNi-MOFs for enhanced oxygen evolution electrocatalysis. Adv Funct Mater, 2021, 31: 2103318
42 Cai Z, Wang P, Zhang J, *et al.* Reinforced layered double hydroxide oxygen-evolution electrocatalysts: A polyoxometallic acid wet-etching approach and synergistic mechanism. Adv Mater, 2022, 34: 2110696
43 Dionigi F, Zhu J, Zeng Z, *et al.* Intrinsic electrocatalytic activity for oxygen evolution of crystalline 3d-transition metal layered double hydroxides. Angew Chem Int Ed, 2021, 60: 14446–14457
44 Chi H, Wang J, Wang H, *et al.* Super-stable mineralization of Ni^{2+} ions from wastewater using CaFe layered double hydroxide. Adv Funct Mater, 2021, 32: 2106645
45 Yilmaz G, Yam KM, Zhang C, *et al. In situ* transformation of MOFs into layered double hydroxide embedded metal sulfides for improved electrocatalytic and supercapacitive performance. Adv Mater, 2017, 29: 1606814
46 Abellán G, Coronado E, Martí-Gastaldo C, *et al.* Photo-switching in a hybrid material made of magnetic layered double hydroxides intercalated with azobenzene molecules. Adv Mater, 2014, 26: 4156–4162
47 Song M, Zhou G, Lu N, *et al.* Oriented attachment induces fivefold twins by forming and decomposing high-energy grain boundaries. Science, 2020, 367: 40–45
48 Li D, Nielsen MH, Lee JRI, *et al.* Direction-specific interactions control crystal growth by oriented attachment. Science, 2012, 336: 1014–1018
49 Li L, Chen W, Luo W, *et al.* $Co_{0.5}Ni_{0.5}MoO_4$ double-shelled hollow spheres with enhanced electrochemical performance for supercapacitors and lithium-ion batteries. Energy Technol, 2019, 7: 1801160
50 Qin M, Zhang L, Zhao X, *et al.* Lightweight Ni foam-based ultrabroadband electromagnetic wave absorber. Adv Funct Mater, 2021, 31: 2103436
51 Tan M, Ma Y, Yu C, *et al.* Boosting photocatalytic hydrogen production *via* interfacial engineering on 2D ultrathin Z-scheme $ZnIn_2S_4$/g-C_3N_4 heterojunction. Adv Funct Mater, 2021, 32: 2111740
52 Xiang J, Zhang T, Cao R, *et al.* Optimizing the oxygen vacancies concentration of thin NiO nanosheets for efficient selective CO_2 photoreduction. Sol RRL, 2021, 5: 2100703
53 Zhuang G, Chen Y, Zhuang Z, *et al.* Oxygen vacancies in metal oxides: Recent progress towards advanced catalyst design. Sci China Mater, 2020, 63: 2089–2118
54 Gong E, Ali S, Hiragond CB, *et al.* Solar fuels: Research and development strategies to accelerate photocatalytic CO_2 conversion into hydrocarbon fuels. Energy Environ Sci, 2022, 15: 880–937
55 Qi L, Zheng Z, Xing C, *et al.* 1D nanowire heterojunction electrocatalysts of $MnCo_2O_4$/GDY for efficient overall water splitting. Adv Funct Mater, 2021, 32: 2107179
56 Xie Z, Xu Y, Li D, *et al.* Covalently bonded Bi_2O_3 nanosheet/Bi_2WO_6 network heterostructures for efficient photocatalytic CO_2 reduction. ACS Appl Energy Mater, 2020, 3: 12194–12203
57 Sun B, Qiu P, Liang Z, *et al.* The fabrication of 1D/2D CdS nanorod@Ti_3C_2 MXene composites for good photocatalytic activity of hydrogen generation and ammonia synthesis. Chem Eng J, 2021, 406: 127177
58 Chen W, Han B, Tian C, *et al.* MOFs-derived ultrathin holey Co_3O_4 nanosheets for enhanced visible light CO_2 reduction. Appl Catal B-Environ, 2019, 244: 996–1003
59 Jiang S, Liu J, Zhao K, *et al.* Ru(bpy)$_3^{2+}$-sensitized {001} facets $LiCoO_2$ nanosheets catalyzed CO_2 reduction reaction with 100% carbonaceous products. Nano Res, 2021, 15: 1061–1068
60 Tan L, Xu SM, Wang Z, *et al.* Highly selective photoreduction of CO_2 with suppressing H_2 evolution over monolayer layered double hydroxide under irradiation above 600 nm. Angew Chem Int Ed, 2019, 58: 11860–11867
61 Wang XK, Liu J, Zhang L, *et al.* Monometallic catalytic models hosted in stable metal-organic frameworks for tunable CO_2 photoreduction. ACS Catal, 2019, 9: 1726–1732
62 Zhou L, Chen FF, Chen J, *et al.* Highly dispersive Ni@C and Co@C nanoparticles derived from metal-organic monolayers for enhanced photocatalytic CO_2 reduction. Inorg Chem, 2021, 60: 10738–10748
63 Lin X, Wang S, Tu W, *et al.* Magnetic hollow spheres assembled from graphene-encapsulated nickel nanoparticles for efficient photocatalytic CO_2 reduction. ACS Appl Energy Mater, 2019, 2: 7670–7678
64 Liang S, Liu X, Zhong Z, *et al.* Lattice-strained nanotubes facilitate efficient natural sunlight-driven CO_2 photoreduction. Nano Res, 2020, 14: 2558–2567
65 Han B, Song J, Liang S, *et al.* Hierarchical $NiCo_2O_4$ hollow nanocages for photoreduction of diluted CO_2: Adsorption and active sites engineering. Appl Catal B-Environ, 2020, 260: 118208
66 Han B, Ou X, Zhong Z, *et al.* Rational design of FeNi bimetal modified covalent organic frameworks for photoconversion of anthropogenic CO_2 into widely tunable syngas. Small, 2020, 16: 2002985
67 Zhong W, Sa R, Li L, *et al.* A covalent organic framework bearing single Ni sites as a synergistic photocatalyst for selective photoreduction of CO_2 to CO. J Am Chem Soc, 2019, 141: 7615–7621
68 Chen W, Liu X, Han B, *et al.* Boosted photoreduction of diluted CO_2 through oxygen vacancy engineering in NiO nanoplatelets. Nano Res, 2020, 14: 730–737
69 Salzmann BBV, van der Sluijs MM, Soligno G, *et al.* Oriented attachment: From natural crystal growth to a materials engineering tool. Acc Chem Res, 2021, 54: 787–797
70 Penn RL, Banfield JF. Imperfect oriented attachment: Dislocation generation in defect-free nanocrystals. Science, 1998, 281: 969–971
71 Liu Y, Che R, Chen G, *et al.* Radially oriented mesoporous TiO_2 microspheres with single-crystal-like anatase walls for high-efficiency optoelectronic devices. Sci Adv, 2015, 1: e1500166
72 Liu L, Nakouzi E, Sushko ML, *et al.* Connecting energetics to dynamics in particle growth by oriented attachment using real-time observations. Nat Commun, 2020, 11: 1045
73 Pathiraja G, Herr DJC, Rathnayake H. Nanoscopic insight into sol-gel chemical kinetics of oriented attachment crystal growth in anisotropic copper hydroxide nanowires. Cryst Growth Des, 2022, 22: 2889–2902
74 Liu Y, Geng H, Qin X, *et al.* Oriented attachment revisited: Does a chemical reaction occur? Matter, 2019, 1: 690–704
75 Guo J, Cao Y, Shi R, *et al.* A photochemical route towards metal sulfide nanosheets from layered metal thiolate complexes. Angew Chem Int Ed, 2019, 58: 8443–8447
76 Arora D, Tan HR, Wu WY, *et al.* 2D-oriented attachment of 1D colloidal semiconductor nanocrystals *via* an etchant. Nano Lett, 2022, 22: 942–947
77 Jeon S, Jung MC, Ahn J, *et al.* Post-synthetic oriented attachment of $CsPbBr_3$ perovskite nanocrystal building blocks: From first principle calculation to experimental demonstration of size and dimensionality (0D/1D/2D). Nanoscale Horiz, 2020, 5: 960–970
78 Cheng F, Lian L, Li L, *et al.* Hybrid growth modes of PbSe nanocrystals with oriented attachment and grain boundary migration. Adv Sci, 2019, 6: 1802202
79 Zhu C, Liang S, Song E, *et al. In-situ* liquid cell transmission electron

microscopy investigation on oriented attachment of gold nanoparticles. Nat Commun, 2018, 9: 421

Acknowledgements This work was financially supported by the National Key Research and Development Program/Key Scientific Issues of Transformative Technology (2020YFA0710303), the National Natural Science Foundation of China (U1905215 and 52072076), Fujian Natural Science Foundation (2022J01554), and the Key Project of Science and Technology Innovation of Fujian Provincial Department of Education (2022G02002).

Author contributions Zhang T, Zhao X, Zhuang Z and Yu Y designed and adjusted the experimental plan; Zhang T and Zhao X performed the experiments; Lin M, Yang B and Yan J performed the theoretical calculations. Zhang T, Zhao X, Zhuang Z and Yu Y wrote the paper. All authors contributed to the general discussion.

Conflict of interest The authors declare that they have no conflict of interest.

Supplementary information Supporting data are available in the online version of the paper.

Tingshi Zhang received his BS degree in materials science and engineering from Fuzhou University, and he is currently working for his PhD degree at Fuzhou University under the supervision of Prof. Yu and Prof. Zhuang. His research focuses on the design of 2D nanomaterials catalysts and related catalytic topics.

Xin Zhao is presently a Master's student at the School of Materials Science and Engineering, Fuzhou University. His research interests focus on the design of nickel-based catalysts for heterogeneous photocatalysis.

Zanyong Zhuang received his BS degree (2006) in chemistry from Xiamen University and his PhD degree (2011) from Fujian Institute of Research on the Structure of Matter (FJIRSM), Chinese Academy of Sciences (CAS). Currently, he is a full professor at Fuzhou University. His research interests mainly focus on the rational design of transition metal-based catalysts for energy and environmental applications, including advanced oxidation reaction and CO_2 reduction reaction.

Yan Yu received her BS, MS, and PhD degrees from Fuzhou University. During 2010–2013, she was a postdoctoral fellow at FJIRSM, CAS. Currently, she is a professor at Fuzhou University. Her research interests include environmental remediation, water purification, ecological materials, photocatalytic CO_2 reduction, and H_2 production.

无表面活性剂定向一维/二维NiZn-LDH异质结实现100%高效选择性光催化CO_2还原

张庭士[1,2†], 赵鑫[1,2†], 林铭雄[1,2], 杨碧霞[1,2], 颜家伟[1,2], 庄赞勇[1,2*], 于岩[1,2*]

摘要 构建高度定向、有序的一维/二维异质结催化材料是解决能源和环境危机的重要途径. 本工作报道了在不添加表面活性剂条件下, 纳米层状双金属氢氧化物(NiZn-LDHs)可以在生长过程中自发调控其生长晶面, 并通过一种非经典取向结合生长机制, 形成高度定向、有序的一维/二维异质结构. 定向、有序异质结结构的形成源于一维NiZn-LDH纳米针的(101)面和二维NiZn-LDH纳米片的(100)面之间的晶格匹配. 定向、有序异质结结构促使一维基元在二维基元上高度分散, 而高度分散的一维NiZn-LDH富含缺陷, 具有较强的CO_2吸附和活化能力. 定向一维/二维异质结强化了一维和二维基元之间的相互作用, 可加速光生电子从二维基元向含活性位点一维基元的定向传输, 赋予催化材料优异的可见光光催化还原CO_2性能(CO的产出速率达16,950 μmol g^{-1} h^{-1}; CO选择性高达100%). 本工作展示了各向异性纳米结构材料可以自发调控其生长行为, 为高效、定向、有序的异质结催化材料的设计提供了新的思路.

